X-dimensional Mass Spectrometry Imaging Discovers Spatially Resolved Metabolic Response

Xiaowei Song
Chinese Academy of Medical Sciences and Peking Union Medical College
Qingce Zang
State Key Laboratory of Bioactive Substance and Function of Natural Medicines, Institute of Materia Medica, Chinese Academy of Medical Sciences and Peking Union Medical College, Beijing 100050
Jin Zhang
Institute of Materia Medica, Chinese Academy of Medical Sciences and Peking Union Medical College
Shanshan Gao
Institute of Materia Medica, Chinese Academy of Medical Sciences and Peking Union Medical College
Kailu Zheng
Institute of Materia Medica, Chinese Academy of Medical Sciences and Peking Union Medical College
Yan Li
Institute of Materia Medica, Chinese Academy of Medical Sciences and Peking Union Medical College
Zeper Abliz (zeper@muc.edu.cn)
Minzu University of China https://orcid.org/0000-0002-4876-2392
Jiuming He
Institute of Materia Medica, Chinese Academy of Medical Sciences and Peking Union Medical College
https://orcid.org/0000-0002-6545-472X

Article

Keywords:

Posted Date: March 15th, 2022

DOI: https://doi.org/10.21203/rs.3.rs-1432835/v1

X-dimensional Mass Spectrometry Imaging Discovers Spatially Resolved Metabolic Response

Xiaowei Song[1,2#], Qingce Zang[1#], Jin Zhang[1#], Shanshan Gao[1], Kailu Zheng[1,3], Yan Li[1,3], Zeper Abliz[1,4,5 *], Jiuming He[1,6*]

1. State Key Laboratory of Bioactive Substance and Function of Natural Medicines, Institute of Materia Medica, Chinese Academy of Medical Sciences and Peking Union Medical College, Beijing 100050, China

2. Department of Chemistry, Fudan University, 200438, Shanghai, China

3. Beijing Key Laboratory of New Drug Mechanisms and Pharmacological Evaluation Study, Institute of Materia Medica, Chinese Academy of Medical Sciences and Peking Union Medical College, Beijing, 100050, China

4. Key Laboratory of Mass Spectrometry Imaging and Metabolomics, Minzu University of China, National Ethnic Affairs Commission, Beijing 100081, China

5. Key Laboratory of Ethnomedicine of Ministry of Education, School of Pharmacy, Minzu University of China, Beijing 100081, China

6. NMPA Key Laboratory of safety research and evaluation of Innovative Drug, Institute of Materia Medica, Chinese Academy of Medical Sciences and Peking Union Medical College, Beijing 100050, China

# These authors contribute equally.

*Correspondence:

Jiuming He, hejiuming@imm.ac.cn; Zeper Abliz, zeper@imm.ac.cn

This study developed an open-source method, x-dimensional mass spectrometry imaging (MSI$^{(x)}$), to reveal the spatially-resolved high-order metabolomics information associated with disease progression or drug action. This high order bioinformation includes metabolism pathway, species, biofunction, or biotransformation, which involves multiplex metabolites and cannot be presented by a single ion image. The MSI$^{(x)}$ enables the evaluation of the physiological status, the discovery of therapeutic or adverse effects, the investigation of regional heterogeneous response to drug treatment, possible molecular mechanism, and even drug potential target. MSI$^{(x)}$ was demonstrated to be a promising molecular imaging tool not only for efficacy and safety evaluation but also for the molecular mechanism investigation at the early stage of drug research and development.

Introduction

Mass spectrometry imaging (MSI) has become a powerful molecular mapping tool in the fields of biology[1,2], medicine[3,4], and pharmacy[5,6]. With the aid of a variety of ionization sources operated under vacuum or ambient atmospheric condition (e.g. MALDI, SIMS, DESI, LA-ESI), MSI technique has been successfully applied to detect synthetic drugs, metabolites, lipids, peptides, proteins, metals, glycans, *etc*[7,8,9,10]. A multiplex molecular changes caused by disease progression or drug intervention can be visualized at the whole-body, organ, tissue, cell or even sub-cellular resolution[11, 12, 13,14]. This unique advantage in spatially resolved multiplex molecular detection makes MSI promising in drug research and development (R&D)[15,16].

The drug R&D is a time- and cost-consuming journey to screen one compound out of thousands of chemical entities[17,18]. As a qualified drug candidate, its therapeutic and adverse effect as well as potential target and molecular mechanism are major concerns to decide the further development or suspension at the early stage[19,20,21]. All these information can be precisely described by their downstream metabolic profile disturbance (termed as "perturbation") [22,23] and well characterized by the MSI technique.

A drug's influence on the disease progression often involves an orchestrated metabolic response involving multiplex molecules. Some of functional metabolites behave distinctive or even opposite change tendencies[24,25]. In this circumstance, the drug's complex influence cannot be comprehensively described by any single indicating metabolite. There is still many advanced metabolomics information need to be visually explored such as general metabolic profile, pathways, species, functions, and biotransformation. These high order bioinformation is critical for the drug's efficacy/safety evaluation and mechanism interpretation, but hard to be directly read out from mass spectra or a single ion image. A new synthetic metric needs to be constructed beyond metabolite ion intensity for presenting this spatially resolved biological information.

Inspired by machine learning and chemometrics techniques[26,27,28], we proposed a metric, metabolic perturbation score (MPS), to characterize the extent of the drug's action and spotlight its impact region across the whole body and heterogenous tissue. We hypothesize that the MPS can be presented by the inter-group distance in the feature space, which should be

highly associated with the drug's action. Given a library that includes every metabolite ion's exact *m/z* value and biological function annotation, a drug's influence on any specific pathway, species, biological function, or transformation can also be measured. We termed the constructed map of MPS at the pixel basis as the "x-dimensional image" and this open-source, exploratory MSI method as "x-dimensional mass spectrometry imaging" ($MSI^{(x)}$).

In this study, our self-developed ambient ionization method, air-flow-assisted desorption electrospray ionization mass spectrometry (AFADESI) [29,30] was employed to conduct the spatially resolved higher-order metabolomics on the whole-body animal (WBA) under a polarity-switching mode. The general workflow is presented in **Fig 1,** and this MSI function is demonstrated to be powerful in displaying these spatially resolved metabolic response to the drug action or disease progression pattern beyond single ion image.

RESULTS

Preparation for $MSI^{(x)}$ analysis. Matrix construction for spatially resolved metabolomics data, the custom-library buildup, and spatial segmentation are three prerequisites for further $MSI^{(x)}$ analysis. The spatial metabolomics data was collected from 7 different groups of WBA cryosections. Peak inclusion procedure preserved 1083 positive and 1347 negative ions to present the untargeted metabolomic profile. Afterward, a pretrained K-nearest neighboring (KNN) model was introduced to delineate histological regions of WBA and its tumor according to metabolic profile features. Its performance was tested on 12764 WBA image pixels and 14570 tumor image pixels through 10-fold cross-validation. An over 90 % prediction accuracy can be achieved for the histological region prediction for each pixel (**supplementary Fig. S1-S2**). Finally, each WBA matrix was divided into 15 sub-matrices whereas each tumor matrix was split into 3 sub-matrices (**supplementary Fig. S3-S4**). Those submatrices derived from the same type were re-combined as a new regional matrix for the distance measurement and MPS image reconstruction, respectively. A customized library was built on identified metabolite ions detected by AFADESI-MSI. There were 869 metabolite entries (1815 positive and negative ions) categorized into 62 different types of metabolism pathway, chemical species, biological function,

or biotransformation (**supplementary Table 1,** and **Fig. S5)**. All the information is referenced from the Kyoto Encyclopedia of Genes and Genomes (KEGG: https://www.genome.jp/kegg/). Given accurately assigned pixel labels and customized library, any set of interested metabolite ions on a specific region can be accessed to investigate the drug action pattern by MSI$^{(x)}$.

MSI$^{(x)}$ predicts drug action sites and evaluates physiological status. Taking MPS as the metric, x-dimensional images were first used to compare the disturbance of general metabolic profile at the WBA level after different drug treatments. Regions that gain higher MPS values can be highlighted in the x-dimensional image. As a result, compared to the normal control (NC) group, multiple regions including liver, spleen, brain, and muscle achieved higher perturbation scores in the tumor model contrast (MC) group (**Fig.2a**). This indicated that the cancer advancing probably dysregulated the metabolism of these organs or tissue. By contrast, the MPS in the brain, liver, and muscle regions of the paclitaxel (PTX), paclitaxel derivative 1 (PTR), and paclitaxel derivative 2 (PTS) groups have been obviously tuned back (**Supplementary Fig.S6**), indicating the partial recovery of the metabolism status because of the drug intervention. Additionally, the intestine region from the PTX had the highest MPS compared to other groups, meaning that PTX may cause serious adverse effects to the digestion, absorption, and excretion system. These results got support from the body weight curve showing the PTX group animals had the sharpest loss in body weight (**Supplementary Fig.S7**). It also indicated the two PTX derivatives, PTR, and PTS (particularly in low dosage) can effectively reduce the severe toxicity of PTX to the body's physiological status.

MSI$^{(x)}$ characterizes the dose-activity dependency. From WBA perturbation images, it can be apparently observed that spleens from three PTS-treated groups were highlighted to be the region with the highest metabolic profile change (**Fig. 2a**). Furthermore, the spleen MPS values in the PTS group increased with the dosage. This dose-action dependency was supported by their corresponding spleen indexes after pharmacological trial (negative correlation, r = 0.99, **Fig.2b**). The ELISA test on serum also revealed significantly changed levels in several antibodies and immune factors such as IgA, IgG, IFN-γ, TNF-α, IL-6, and IL-10 after drug intervention (**Fig.2b**, and **supplementary Fig. S8**). We then analyzed the correlation

between serum IgA, and IgG levels and the four groups that have apparent metabolic perturbation on the spleen region (model, PTS (L), PTS (M), and PTS (H)). Surprisingly, the spleen MPS values were in high agreement with the corresponding serum IgA (positive correlation, r= 0.86), IgG (positive correlation, r=0.87), TNF-α (negative correlation, r=0.99), IFN-γ (negative correlation, r=0.96), IL-10 (positive correlation, r=0.92), IL-6 (negative correlation, r=0.98), (**Fig. 2b**, and **supplementary Fig. S8**). These results gave more valid proof that the spleen was the potential PTS action site and responsible for these immune factors changes. It also demonstrated that the $MSI^{(x)}$ method could trace the primary region of a drug action underlying biochemical markers changes at the global circulation level.

$MSI^{(x)}$ evaluates the organ's metabolic function. We further investigated the use of $MSI^{(x)}$ in evaluating the drug's influence on the function of the liver, which is the most important organ involved in metabolism. Two sets of metabolites, alanine and pyruvate, aspartate, and glutamate, were selected because they are the substrates and products of alanine transaminase (ALT) and aspartate transaminase (AST), two important enzyme markers used for evaluating liver metabolism function (**supplementary Fig. S9**). The x-dimension image of metabolic perturbation (**Fig. 2c**) revealed that the liver metabolism function was significantly influenced by every treated group compared to NC. This result got the support of biochemical validation through the ELISA tests on serum AST and ALT expression levels (**Fig. 2d**). There were also certain extents of positive correlation between the serum AST, ALT, and the liver MPS values in groups of NC, PTX, PTR, PTS (L), PTS (M), and PTS (H) (**Fig. 2e**).

$MSI^{(x)}$ presents the tumor heterogenetic metabolic response. After safety evaluation, drugs' therapeutic efficacies at the solid tumor region were also investigated. Cryosections were first gone through the H&E staining for guiding tumor sub-regions (**Fig. 3a**). We then conducted the $MSI^{(x)}$ analysis on every sub-region. Given an inquiry vector consisting of highly related metabolite ion locations in the library, any specific metabolic profile presenting a function, species, transformation, or pathway can be easily generated for direct comparison (**Fig. 3b**). There were multiple metabolic phenotype changes in tumor after the drug intervention (**supplementary Table S2**). Taking energy metabolism as an example, a couple of metabolites involved in the Krebs cycle showed decreased tendencies

particularly lactate, fumarate, and glucose (**supplementary Fig. S10**), indicating the suppression of cancer cells' energy consumption after treatment with PTX, PTR, and PTS.

Some spatially resolved high-order metabolomics changes were visualized including Krebs cycle (function), cysteine, and methionine metabolism (pathway), glycerophospholipids (GPL, species), and methylation (transformation). From the MC group, the Krebs cycle and methylation were more active across the outer periphery of the parenchyma region whereas the methionine and cysteine metabolism, and GPL species were more intense in the inner parenchyma region. After drug intervention, the Krebs cycle activity, GPL abundance, and methylation level were all downregulated but the methionine, and cysteine metabolism seem to be upregulated (**Fig. 3c**).

We then plotted the microregion-specific pixel's metabolic perturbation in the 2D t-SNE feature space. A shift off the MC group was observed from the sample points of necrosis and parenchyma other than stroma region in every drug-treated group (**Fig. 3d, 3e,** and **3f**), indicating the tumor heterogenetic response. This shift could also represent the drug's influence on the tumor metabolism which is supported by the tumor weight plot revealing that PTX, PTR, and PTS all significantly inhibit the tumor growth (**Fig. 3g**). It can be concluded that the parenchyma and necrosis regions showed the more sensitive metabolic response compared to the stroma region.

MSI$^{(x)}$ investigates molecular mechanism. Replicates of tumor sections (n=3) were separately analyzed by MSI$^{(x)}$ to get their metabolic perturbation images. A highly consistent result can be achieved within each group, proving the repeatability of MSI$^{(x)}$ and individual variation in metabolic profile changes (**Fig. 4a**). To gain an in-depth understanding of the drug's action mechanism, more details about drug-caused metabolic perturbation were systematically studied by investigating 62 various categories of metabolism pathways, species, and bio-transformations recorded in the library. Ranked the top 3 items based on their perturbation scores (**Fig.4b**), it was found that three drugs mainly influence the methylation processes and lipid utilization. In terms of affected species, phosphatidylcholine (PC) ranked in the first place. Pathways ranking revealed that cysteine and methionine metabolism

achieved the highest perturbation scores. This discovery was supported by the pathway enrichment analysis result given by the Metaboanalyst (http://www.metaboanalyst.ca) [31], which also highlights the same pathway as the most significant alteration by drug action (**supplementary Fig. S11-S22**, and **Table S3**).

Special attention was focused on the one-carbon metabolism and species due to highlights of methylation, phosphatidylcholine, cysteine, and methionine metabolism by MSI$^{(x)}$ analysis. Methylation is an epigenetic modification that plays a vital role in regulating biochemical processes during cancer cell proliferation such as GPL synthesis [32,33]. The methylation process was conducted by the S-adenosylmethionine (SAM)/S-adenosylhomocysteine (SAH) conversion with the methionine as the donor for one-carbon unit [34,35]. Additionally, the synthesis of PC also heavily relies on the methylation of phosphatidylethanolamine (PE) under the aid of SAM/SAH conversion. Both PC and PE are key components for constructing bilayer membranes of cell and organelles.

MSI$^{(x)}$ localizes potential drug targets. Based on the reasoning above, we postulated that paclitaxel derivatives may cause an inhibitive influence on the methionine cycle mediated one-carbon unit transport and utilization for the PE/PC conversion (**Fig.4c**). The S-adenosylmethionine synthase (MAT) involves in SAM generation from methionine whereas the PEMT catalyzes methylation reaction of PE to produce PC species[36,37,38,39]. Therefore, these two enzymes were highly suspicious to be the key target that the drug could have significant influence associated with the tumor progression. From the metabolite ion images, we can observe that the abundances of methionine, and PE(34:1) were increased whereas the SAM and PC(34:1) were decreased in three drug-treated groups compared to the MC group (**Fig. 4d**). This result supported our presumption that the cancer proliferation gets inhibited due to lack of the SAM supply and thereby methyl group transfer for PE/PC conversion. The expression of MAT in tumor sections was also validated by immunohistochemistry (IHC), confirming that PTS has significant inhibition over PTX and PTR (**Fig. 4e-4f**). The only pity thing is that no significant different was observed from the PEMT expression among groups.

We also investigated the correlation between local drug amount and methionine in tumors. Average intensities of PTS, PTX, and methionine from representative regions of interest in parenchyma were extracted for linear fitting. As a result, the amount of methionine can be highly related to the PTS (positive correlation, r = 0.82) other than PTX (r = 0.12) in the parenchyma, indicating that the prodrug PTS itself may also have a distinctive influence on cysteine and methionine metabolism (**Fig. 4g-4h,** and **supplementary Figure S23**). Additionally, we also noticed that PTS cause the greatest changes in abundance for cysteine, 3-sulfinoalanine, serine, and homocysteine which are also located in the cysteine and methionine pathway (**supplementary Fig. S24**). These phenomena made us believe that PTS itself serves as a distinctive active entity other than its free form PTX.

DISCUSSION

The performance of MSI$^{(x)}$ method heavily relies on the sensitivity of the employed ionization method. In this study, the AFADESI-MSI was introduced to implement spatial metabolomics data acquisition. After a decade of efforts in its hardware upgrading[29,30], software development[40, 41], and methodology studies [42, 43, 44, 45], the detection sensitivity improvement has been remarkably achieved on this platform to widely cover various types of metabolites. In the drug's anti-tumor efficacy study, there were 869 target metabolites (1816 positive and negative ions) involved in 62 different types of metabolism pathways, species, and biotransformation in the metabolite ion library. The excellent performance of AFADESI guarantees the feasibility of MSI$^{(x)}$ method in evaluating the drug's specific action sites in the metabolism network[46].

When comparing the spatial metabolomics among different treated groups, spatial segmentation is another critical step especially for the heterogenous tissue like tumor and highly structural organs or whole-body animal. Only in this way, it can be ensured that the metabolic profiles are compared within the same type of region and the difference caused by region-specific molecular composition can be ruled out. With aid of a machine learning model, all sample points can be accurately labeled as different region types for statistical analysis and distance measurement in the feature space separately.

The synthetic metric built on multiple metabolites centered to certain biological function could give a more comprehensive and biologically interpretable elucidation over a single metabolite marker. In this research, the serum AST and ALT levels in model and drug treated groups have different extents of upregulation compared to the normal control group. This trend cannot be reflected either by images of glutamate, aspartate, alanine, and pyruvate, or the product/substrate ratio images (**supplementary Fig. S25**). Instead, the image of metabolic perturbation score based on the panel of these 4 functional metabolites have highly consistent trend with the results of blood AST and ALT assay.

$MSI^{(x)}$ provides a novel metric to objectively reflect the spatially resolved perturbation not only to the general metabolic profile but also to the specific metabolite groups of interest. This study gave a proof-of-concept demonstration that the spatial metabolic perturbation-based score can be highly associated with the drug's actions including the therapeutic and adverse effects. Thus, it has biological interpretability when evaluating the drug's efficacy and safety at the stage of preclinical drug research and development.

To measure the metabolic perturbation and narrow the search scope of metabolism pathways, selecting the metabolites of interest is a necessary step to construct the feature vector and sub-matrix for spatially resolved metabolomics study. These metabolites were not only successfully detected in our previous studies but also involved in various pathways and served as important biological functions[47,48,49]. Metabolite entries that a feature vector includes can be freely combined according to the user's specific purpose. More importantly, the metabolite reference library is also extensible by creating new metabolite entries for expanding the search range and new biological function exploratory.

The presented method enables conventional MSI a new dimension to explore the implicit high-order metabolomics information beyond the molecular composition and relative abundances. It is also worth noting that the $MSI^{(x)}$ method is not merely applicable for the preclinical drug research and development in our self-built AFADESI-MSI system. Theoretically, the feature space can be built on various types of molecules such as metals, lipids, peptides, proteins, or glycans, according to the specific research

purpose and MSI platforms like MALDI, SIMS, nano-DESI, LA-ESI, etc. Therefore, we expect MSI$^{(x)}$ to become a visual characterization mode that has universal applicability in MSI-based studies no matter for proteomics, glycomics, lipidomics, or metabolomics.

ACKNOWLEDGMENTS

The authors are grateful for financial support from the National Natural Science Foundation of China (No. 21927808, 81974500, 81773678, 81903575) and the CAMS Innovation Fund for Medical Sciences (Grant No. 2021-1-I2M-026).

AUTHOR CONTRIBUTIONS

# X.W.S, Q.C.Z, and J.Z contributed equally to this work. J.M.H and Z.A designed the research and supervised all of the research work; Y.L. conducted the pharmacological research; X.W.S. and J.M.H. planned the experiments; K.L.Z, helped to cultivate the cancer cell suspension, prepare the tumor model mouse and made the drug administration; J.Z, S.S.G, K.L.Z, and Y.L. carried out the pharmacological experiment, Q.C.Z conducted the AFADESI-MSI data acquisition and biological validation, X.W.S complete the AFADESI-MSI data analysis process and wrote the manuscript; J.M.H. and Z.A. revised the manuscript.

COMPETING INTERESTS

The authors declare no competing interests.

METHOD

General workflow of the MSI$^{(x)}$ method. The key steps to implement this MSI$^{(x)}$ method are stated as below:

step 1: Collect the untargeted/targeted spatially resolved metabolomics data from a xenografted whole-body animal (WBA) cryosection as much as possible to cover a wide range of metabolite species and construct the metabolomics data matrix.

step 2: Construct a knowledge-based customized library. This library consists of metabolite ions that are involved in various pathways, species, functions, and biotransformation. Given a list of target metabolite ion intensities, $\vec{I} = (I_1, I_2, \ldots I_n)$, any set of featured metabolite ions, $\vec{t} = (t_1, t_2, \ldots t_n)$, can be accessed by dot multiplying with a 1× n inquiry vector, $\vec{v}$ =

$(v_1, v_2, \ldots v_n)$ (equation 1). Each element in the inquiry vector was filled with either "0" or "1", denoting the selection status of correspondent metabolite ion. The "*n*" presents the total number of metabolite ions included in the library.

$$\vec{t} = \vec{v} \cdot \vec{I} \quad (1)$$

step 3: Use a machine learning model to accurately assign every data point (pixel) with a physiological region label and split the intact WBA data matrix into several regional sub-matrices for the following separate data analysis.

step 4: Extract metabolic profile features (t-SNE$_{1\sim3}$) from the high-dimension metabolic profile of each regional matrix. Project all pixels into the metabolic feature space for grouping and further distance measurement.

step 5: Set the centroid position of the control group as the reference point, measure the Euclidean (equation 2) or Mahalanobis (equation 3) distance between each test pixel and the reference point in the feature space. The shorter distance between a sample point and the reference centroid denotes the less metabolic perturbation that sample point was influenced by drug treatment or cancer progression. The Euclidean distance, Mahalanobis distance, and metabolic perturbation score (MPS) calculation are as follows:

$$\textit{Euclidean distance}: \quad D(\vec{t},\vec{r}) = \sqrt{\sum_{i=1}^{k}(t_i - r_i)^2} \quad (2)$$

$$\textit{Mahalanobis distance: } D(\vec{t},\vec{r}) = \sqrt{(\vec{t} - \vec{r})^T S^{-1}(\vec{t} - \vec{r}\,)} \quad (3)$$

The annotation "*t*" and "*r*" denote a pixel from the test group and the centroid point of a set of pixels in the reference group. The "*i*" denotes the ith element in the featured metabolite ion vector $\vec{t}$ or $\vec{r}$. The "*k*" is the number of dimensions to present the metabolic feature space. The "S^{-1}" is the inverse of covariance matrix.

step 6: Compute the average value from pixels' normalized distances (equation 4) to get the metabolic perturbation score (MPS, equation 5) specific to each major physiological region in the tested WBA for comparing the drug action. The calculation is as follows:

$$D_{norm}^{t} = 100 \times \frac{D^t}{D_{max}} \quad (4)$$

$$MPS_{region} = \frac{1}{n} \sum_{t=1}^{n} D_{norm}^{t} \quad (5)$$

Step 7: Register all regional pixel's distance values back into their physical position according to their group label and location index to finally construct the MPS image (also the "x-dimension image").

Peak selection and matrix construction. Initially, each matrix contains 5370 positive and 3552 negative ions (column in a matrix) collected by the AFADESI-MSI under polarity-switching mode. Two exclusion criteria, namely the signal-to-noise ratio (SNR) and positive detection rate (PDR), were introduced to pick metabolite ions. First, an ion is considered to come from background if its intensity ratio between sample versus non-sample region lower than the SNR threshold set at 1.5. Secondly, an ion is treated as the random noise if it is only positively detected among less than 1.0 % sample image pixels. After peak exclusion, 1083 positive and 1347 negative ions were finally preserved. Finally, there were 2430 columns of ions to present the untargeted metabolic profile for each pixel (one sample point, or one row in a matrix).

Pixel registration. After peak selection, a matrix compression was further conducted at the pixel basis according to the sum of ion intensities. There were totally 12764 pixels from 7 WBA matrices and 14570 pixels from 6 tumor matrices preserved for further analysis, respectively. The 7 groups include normal control (NC), model control (MC), paclitaxel (PTX), paclitaxel derivative 1 (PTR), low, medium, and high doses of paclitaxel derivative 2 (PTS (L), (M), (H)). All Pixels across WBA or tumor were registered with triple elements that the first digit denotes the group index, and last two digits denote position indexes (row and column number) for the image reconstruction.

Spatial segmentation. At the stage of model development, the unsupervised machine learning method, t-stochastic neighboring embedding (t-SNE), was first employed to compress the high-dimension metabolomics data into three features ($t\text{-}SNE_{1\text{-}3}$). Afterward, k-means clustering was employed to give a rough predictive label about each pixel's correspondent region. After registering each pixel's label number back to the physical position, spatial segmentation images of WBA and tumor sections were corrected with their optical images (**Supplementary Fig.S4**) to avoid wrong assignment. Given the histological structures of WBA and tumor tissues,

WBA sample image was divided into 15 subregions including heart, liver, spleen, lung, kidney, brain, intestine, stomach, thymus, gland, intestinal contents, muscles, skin, jaw, and bones. The tumor section was segmented into 3 subregions, namely stroma, parenchyma, and necrosis.

Machine Learning. The built-in "tsne" function in the MATLAB was used to complete the dimension reduction and unsupervised machine learning. The MATLAB APP "classification learner" was used for model comparison, training, and spatial segmentation. With the accurately labelled WBA and tumor data as the training and cross-validation (CV) sets, various of supervised classification models were investigated including K-nearest neighboring (KNN), discriminant analysis (DA), supporting vector machine (SVM), decision tree (DT), naïve bayes (NB), neural network (NN), and ensemble learning (EL). The 10-fold CV was conducted to evaluate the pixel prediction accuracy.

Custom-built Spatial Metabolomics Library. This library was built specially for the spatial metabolomics study. The adduct ion types include $[M+H]^+$, $[M+Na]^+$, $[M+K]^+$, $[M+2Na-H]^+$, $[M+2K-H]^+$, $[M+NH_4]^+$, $[M+H-H2O]^+$ under positive mode, and $[M-H]^-$, $[M+Cl]^-$, $[M+Na-2H]^-$, $[M+K-2H]^-$ under negative mode. A sub-matrix (M_x) can be constructed by extracting the specific columns from the original matrix (M_0) according to an inquiry vector X_i (i=1,2,3…1815). Each element in an inquiry vector X_i is a logical value set at either "0" or "1" which denotes excluded or selected ion in the library. For more details about the search items, please see the **supplementary Table S1** or access to http://www.github.com/xaviersoong/x-MSI.

Tumor Model Development. Under sterile conditions, well-grown lewis tumor tissue was cut into pieces and ground, diluted with sterile saline at a ratio of 1:4 to prepare a tumor cell suspension, and then 0.2 ml tumor cell suspension was inoculated subcutaneously in the left axilla of per mouse. (C57BL/6, six weeks, male, 15-17 g, Beijing Vital River Laboratory Animal Technology Co., Ltd.). The administration of tested drugs was initiated when the tumors grow to the size of approximately 3.0 ± 0.5 mm. The whole procedure of cancer cell line implantation was in strict compliance with the ethical code of animal laboratory medicine in the Chinese Academy of Medical Science and Peking Union Medical College.

Pharmacological Trials. There were 42 mice with subcutaneously transplanted tumors recruited in the pharmacological test. The 42 model mice were randomly divided into 6 groups for dosing the placebo (saline), paclitaxel (PTX, 25 mg/kg), paclitaxel derivative 1 (PTR, 43 mg/kg), and low (15 mg/kg), medium (30 mg/kg), and high (43 mg/kg) doses of paclitaxel derivative 2 (PTS (L), PTS (M), PTS (H)). Another 6 healthy mice were included as the normal control (NC) group. During two weeks of the pharmacology experiment, the mouse in each group was given one dose every three days. The weight and tumor size of each object were recorded on the dosing day.

Sample Collection and Preparation. After the pharmacological test, 7 groups of mice were euthanized in a chamber filled with carbon dioxide and then the blood, major organs (heart, liver, spleen, lung, kidney, brain) and solid tumor were harvested according to the experiment animal ethical code. From each group, we also preserved one intact mouse whole body for spatial metabolomics study. First, the whole-body animal (WBA) was soaked into a mold container filled with carboxyl methyl cellulose sodium (CMC-Na, 2.5 %, *w/v*) gel and then frozen under -80 ℃. The WBA section was cryo-sectioned (25 μm) by cryomacrotome (Leica CM 3600XP) and transferred onto an epoxy-gel coated slide aided by an adhesive tape. Solid tumors were cryo-sectioned with the thickness at 12 μm by cryostat (Leica CM 1860) at -20 °C and thaw mounted on the glass slide. All WBA and tumor tissue cryosections were gone through a 6 hours' drying in a precooled vacuum desiccator before use. Images of WBA and tumor cryosections were acquired by a digital scanner (Microtek Scan Maker i360). The hematoxylin-eosin staining (H&E) was conducted on the adjacent tumor tissue sections for anatomical reference.

AFADESI-MSI Setup and Data Acquisition. A Q-Orbitrap mass spectrometer (Q Exactive, Thermo Scientific) was coupled with the AFADESI (AFAI-MSI 100, Victory, China) setup to conduct the $MSI^{(x)}$ analysis. An electrospray ionization (ESI) sprayer was employed for generating microdroplets for tissue components desorption and ionization. Nitrogen (99.995 %) was also introduced into an ESI sprayer as the nebulizing gas. The commercial ESI compartment was modified by plugging into a stainless-steel transport tube (I.D. 3 mm, O.D 4 mm, Length 500 mm) for desorbed ions transmission. A vacuum pump was also incorporated into the custom-

built source to produce the extracting gas for pneumatic assistance of ion remote transport. More details about the AFADESI configuration can be accessed from previous works.[33, 34]

Acetonitrile-water (7:3, v/v) was used as the spraying solvent with a flow rate of 5.0 μL/min. The nebulizing gas pressure and extracting gas flow was set at 0.7 MPa and 45 L/min, respectively. The angle between the ESI sprayer and impacted tissue slide was 56°. The MS inlet capillary temperature was set at 350 °C and the S lens voltage was 60 V. The positive and negative metabolic profiles were acquired by full scan mode within the range of *m/z* 50-1000 in an alternative way. The maximum injection time was set at 200 ms and the AGC target was locked off to keep the scan rate constant. The MSI data were acquired in a continuous line scan mode. The cryosections of whole-body animal and tumor tissue mounted on glass slides were scanned on a 2D electrical moving stage. The raster speed of a 2D electric moving stage was 0.3 mm/sec and the interval between two lines was 0.3 mm.

Raw MSI Data Preprocessing. Raw MSI data files collected from each WBA and tumor were first converted into serial cdf format files by Xcalibur (Thermo Fisher Scientific). Then, they were imported into MassImager (Chemmind Technologies) for accessing image and average mass spectrum of any interested ion and region. Meanwhile, 7 groups of cdf files were also imported into MATLAB 2021a (Mathworks) for further analysis. A MATLAB live code was written to extract all peak intensities from every MS scan and construct a matrix to store WBA or tumor's metabolomics data. The matrix contains metabolic profile information from all pixels across a tissue section. Each row in the matrix represents one pixel acquired from a single MS scan and each column represents one peak binned along the *m/z* axis with the mass tolerance at ± 0.005 Da. Total ion current normalization was implemented to remove the MS system variation. Natural logarithmic transform was conducted to shape the ion intensities into the normal distribution. The univariate scaling was implemented on each matrix for removing the intensity level influence.

Pathway Enrichment Analysis. The metabolites of interest were put into the open-source platform, MetaboAnalyst (https://www.metaboanalyst.ca), to search for significantly changed metabolism pathways. Reactome

(http://reactome.org) was also used to search the biological events that test drugs could influence by metabolism pathway regulation.

Biological Validation. Several biochemical assays were conducted on the collected blood samples by enzyme-linked immune sorbent assay (ELISA) test kits including the white blood cell (WBC), red blood cell (RBC), platelet count (PLT), ratios of lymphocyte, monocyte, and neutrophil. The liver functions tests were conducted by measuring aspartate transaminase (AST), and alanine transaminase (ALT). The immune function was also evaluated by testing immune factors and antibodies like IL-6, IL-10, TNF-α, IFN-γ, IgA, IgG. For the discovered enzyme (MAT, PEMT) associated with the drug action, their expression levels on the tumor tissue cryosections were validated by immunohistochemistry.

Code availability. All codes for MSI$^{(x)}$ method can be implemented under 2021a (Mathworks, Natick, MA, USA) platform installed in a laptop configured with Dell Inspiron 3593 Processor Intel(R) Core (TM) i7-1065G7 CPU @ 1.30GHz 1.50 GHz, RAM 16.0 GB, Windows 10 (version 20H2), 64-bit operating system, x64-based processor. It is freely available for non-commercial use. The source code in the form a live script (composed of part 1, 2, and 3) and a full version of MSI$^{(x)}$ document can be found and downloaded for scientific research purpose from the http://www.github.com/xaviersoong/x-MSI. The whole run time varied from 30-60 minutes in total, including the artificial parameter tuning, and automatic running by the live script codes composed of three parts.

Data availability. All demo data of WBA and tumor metabolomics described in our study can be downloaded from the Open-Source Framework platform (OSF, https://osf.io/tgvyn, GNU General Public License (GPL) 3.0, for more details, see the documents attached online). All other data supporting the findings of this study are available from the corresponding author on reasonable request.

REFERENCES

1. Tobias F, et al. Developing a Drug Screening Platform: MALDI-Mass Spectrometry Imaging of Paper-Based Cultures. Anal Chem 91, 15370–15376 (2019).

2. Leon M, et al. Metabolites and Lipids Associated with Fetal Swine Anatomy via Desorption Electrospray Ionization - Mass Spectrometry Imaging. Sci Rep 9, 7247 (2019).

3. Eberlin LS, et al. Visualizing Dermal Permeation of Sodium Channel Modulators by Mass Spectrometric Imaging. J Am Soc Chem 136, 6401-6405 (2014).

4. Sun C, et al. Spatially resolved metabolomics to discover tumor-associated metabolic alterations. Pro Nat Acad Sci 116, 52-57 (2019).

5. Luo Z, et al. Whole-body spatially-resolved metabolomics method for profiling the metabolic differences of epimer drug candidates using ambient mass spectrometry imaging. Talanta 202, 198–206 (2019).

6. Margulis K, Margulis K, Neofytou EA, Beygui RE, Zare RN. Celecoxib Nanoparticles for Therapeutic Angiogenesis. ACS Nano 9, 9416–9426 (2015).

7. Ellis SR., et al. Automated, parallel mass spectrometry imaging and structural identification of lipids. Nat Met 15, 515-518 (2018).

8. Wood EA., et al. Neuropeptide localization in Lymnaea stagnalis: From the central nervous system to subcellular compartments. Front Mol. Neurosci. 14 (2021).

9. Maciel L, et al. A new approach for the analysis of amino acid neurotransmitters in mouse brain tissues using DESI imaging. Int. J Mass Spectrom 471, 116730 (2022).

10. McDowell CT, et al. Imaging Mass Spectrometry and Lectin Analysis of N-Linked Glycans in Carbohydrate Antigen–Defined Pancreatic Cancer Tissues. Mol Cell Proteom 1, 20 (2021).

11. Luo Z, et al. Air Flow-Assisted Ionization Imaging Mass Spectrometry Method for Easy Whole-Body Molecular Imaging under Ambient Conditions. Anal Chem 85, 2977-2982 (2013).

12. Lamont L, et al. Targeted Drug and Metabolite Imaging: Desorption Electrospray Ionization Combined with Triple Quadrupole Mass Spectrometry. Anal Chem 90, 13229-13235 (2018).

13. Rappez L, et al. SpaceM reveals metabolic states of single cells. Nat Met 18, 799–805 (2021).

14. Yuan Z, et al. SEAM is a spatial single nuclear metabolomics method for dissecting tissue microenvironment. Nat Met 18, 1223–1232 (2021).

15. Karlsson O, Hanrieder J. Imaging mass spectrometry in drug development and toxicology. Arch Toxicol 91, 2283-2294 (2017).

16. Nilsson A, et al. Mass Spectrometry Imaging in Drug Development. Anal Chem 87, 1437-1455 (2015).

17. Dahlin JL, Inglese J, Walters MA. Mitigating risk in academic preclinical drug discovery. Nat Rev Drug Discov 4, 279-294 (2015).

18. Verkman AS. Drug discovery in academia. Am J Physiol Cell Physiol 286, C465–C474 (2004).

19. Jorgensen WL. Challenges for Academic Drug Discovery. Angew Chem Int Ed 51, 11680–11684 (2012).

20. Kola I. The State of Innovation in Drug Development. Clin Pharmacol Ther 83, 227-230 (2008).

21. Rita Santos, et al. A comprehensive map of molecular drug targets. Nat Rev Drug Discov 16, 19-34 (2017).

22. Fiehn O. Metabolomics –the link between genotypes and phenotypes. Plant Mol Biol 48, 155–171 (2002).

23. Jeremy KN, Lindon JC. Metabonomics. Nature 455, 1054-1056 (2008).

24. Randall EC, et al. Integrated mapping of pharmacokinetics and pharmacodynamics in a patient-derived xenograft model of glioblastoma. Nat Commun 9, 4904 (2018).

25. He J. et al. Ambient Mass Spectrometry Imaging Metabolomics Method Provides Novel Insights into the Action Mechanism of Drug Candidates. Anal Chem 87, 5372-5379 (2015).

26. Nico V, Caprioli R, Van de Plas R. Unsupervised machine learning for exploratory data analysis in imaging mass spectrometry. Mass Spectrom. Rev. 39, 245-291 (2020).

27. Fonville JM, et al. Hyperspectral visualization of mass spectrometry imaging data. Anal Chem 85, 1415-1423 (2013).

28. Guo L, et al. Data Filtering and Its Prioritization in Pipelines for Spatial Segmentation of Mass Spectrometry Imaging. Anal Chem 93, 4788-4793 (2021).

29. He J, et al. Air flow assisted ionization for remote sampling of ambient mass spectrometry and its application. Rap Commun Mass Spectrom 25, 843–850 (2011).

30. He J, et al. A Sensitive and Wide Coverage Ambient Mass Spectrometry Imaging Method for Functional Metabolites Based Molecular Histology. Adv Sci 5, 1800250 (2018).

31. Pang Z, et al. MetaboAnalyst 5.0: narrowing the gap between raw spectra and functional insights. Nucleic Acids Res 49, W388-W396 (2021).

32. Michalak EM, Burr ML, Bannister AJ, Dawson MA. The roles of DNA, RNA and histone methylation in ageing and cancer. Nature reviews Molecular cell biology 20, 573-589 (2019).

33. Newman AC, Maddocks ODK. One-carbon metabolism in cancer. Br J Cancer 116, 1499-1504 (2017).

34. Labuschagne CF, van den Broek NJ, Mackay GM, Vousden KH, Maddocks OD. Serine, but not glycine, supports one-carbon metabolism and proliferation of cancer cells. Cell reports 7, 1248-1258 (2014).

35. Sydney M. Sanderson XG, Ziwei Dai, Jason W. Locasale. Methionine metabolism in health and cancer: a nexus of diet and precision medicine. Nat Rev Cancer 19, 625-637 (2019).

36. Cheng M, Bhujwalla ZM, Glunde K. Targeting Phospholipid Metabolism in Cancer. Front Oncol 6, 00266 (2016).

37. Cai J, Sun W, Hwang J, Stain SC, Lu SC. Changes in S-Adenosylmethionine Synthetase in Human Liver Cancer: Molecular Characterization and Significance. Hepatology 24, 1090-1097 (1996).

38.Zinrajh D, Hörl G, Jürgens G, Marc J, Sok M, Cerne D. Increased phosphatidylethanolamine N-methyltransferase gene expression in non-small-cell lung cancer tissue predicts shorter patient survival. Oncology Letters 7, 2175-2179 (2014).

39. Cífková E, et al. Lipidomic and metabolomic analysis reveals changes in biochemical pathways for non-small cell lung cancer tissues. Biochim Biophys Acta Mol Cell Biol Lipids 1867, 159082 (2022).

40. He J, et al. MassImager: A software for interactive and in-depth analysis of mass spectrometry imaging data. Anal Chim Acta 1015, 50-57 (2018).

41. Huang L, et al. A graphical data processing pipeline for mass spectrometry imaging-based spatially resolved metabolomics on tumor heterogeneity. Anal Chim Acta 1077, 183-190 (2019).

42. Song X, et al. In Situ Hydrogel Conditioning of Tissue Samples To Enhance the Drug's Sensitivity in Ambient Mass Spectrometry Imaging. Anal Chem 89, 6318-6323 (2017).

43. Song X, et al. Virtual Calibration Quantitative Mass Spectrometry Imaging for Accurately Mapping Analytes across Heterogenous Biotissue. Anal Chem 91, 2838-2846 (2019).

44. Song X, et al. Fabrication of homogenous three-dimensional biomimetic tissue for mass spectrometry imaging. J Mass Spectrom 54, 378–388 (2019).

45. Zang Q, et al. Enhanced On-Tissue Chemical Derivatization with Hydrogel Assistance for Mass Spectrometry Imaging. Anal Chem 93, 15373-15380 (2021).

46. Pang X, et al. Mapping Metabolic Networks in the Brain by Ambient Mass Spectrometry Imaging and Metabolomics. Anal Chem 93, 6746-6754 (2021).

47. Li T, et al. In situ biomarker discovery and label-free molecular histopathological diagnosis of lung cancer by ambient mass spectrometry imaging. Sci Rep 5, 14089 (2015).

48. Mao X, et al. Application of imaging mass spectrometry for the molecular diagnosis of human breast tumors. Sci Rep 6, 21043 (2016).

49. Wang Z, et al. Spatial-resolved metabolomics reveals tissue-specific metabolic reprogramming in diabetic nephropathy by using mass spectrometry imaging. Acta Pharm Sinica B 11, 3665-3677 (2021).

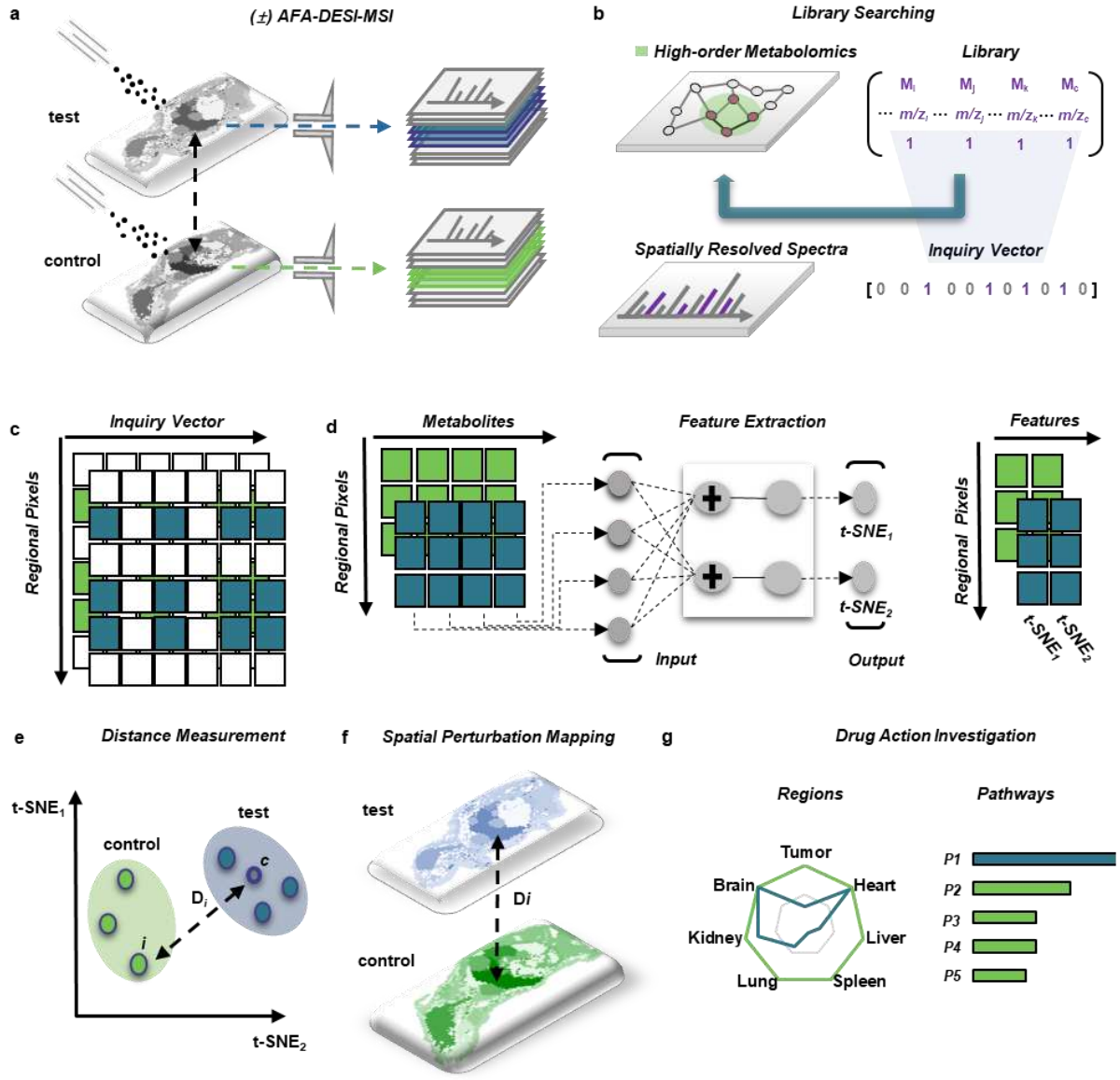

Fig.1. General workflow of MSI$^{(x)}$. a Spatially resolved high-order metabolomics data were first collected from test (red) and control (blue) whole-body animal sections by AFADESI-MSI under a positive/negative switching mode. **b** Given a custom-built library, any set of metabolite ions involved in certain pathway can be accessed from the regional mass spectra by an inquiry vector which element is either coded as "0" or "1". **c** Given a pretrained machine learning model, region-specific metabolomics data from test and control groups can be spliced from the whole matrices and re-constructed to regional matrix. **d** High dimension metabolomics data is compressed and presented by two features (t-SNE1 and t-SNE2). **e** All pixels from two feature matrices are mapped into a 2D feature space and grouped into different clusters. In this feature space, distance of each pixel (*i*) to the control centroid (*c*) is measured. **f** Metabolic perturbation score image across the whole-body animal section is presented by registering all pixels' distance score back to their original location. **g** Metabolic perturbation score of each region was calculated by

averaging all regional pixels' distance**.** The drug action on specific pathway can also be highlighted based on its perturbation score.

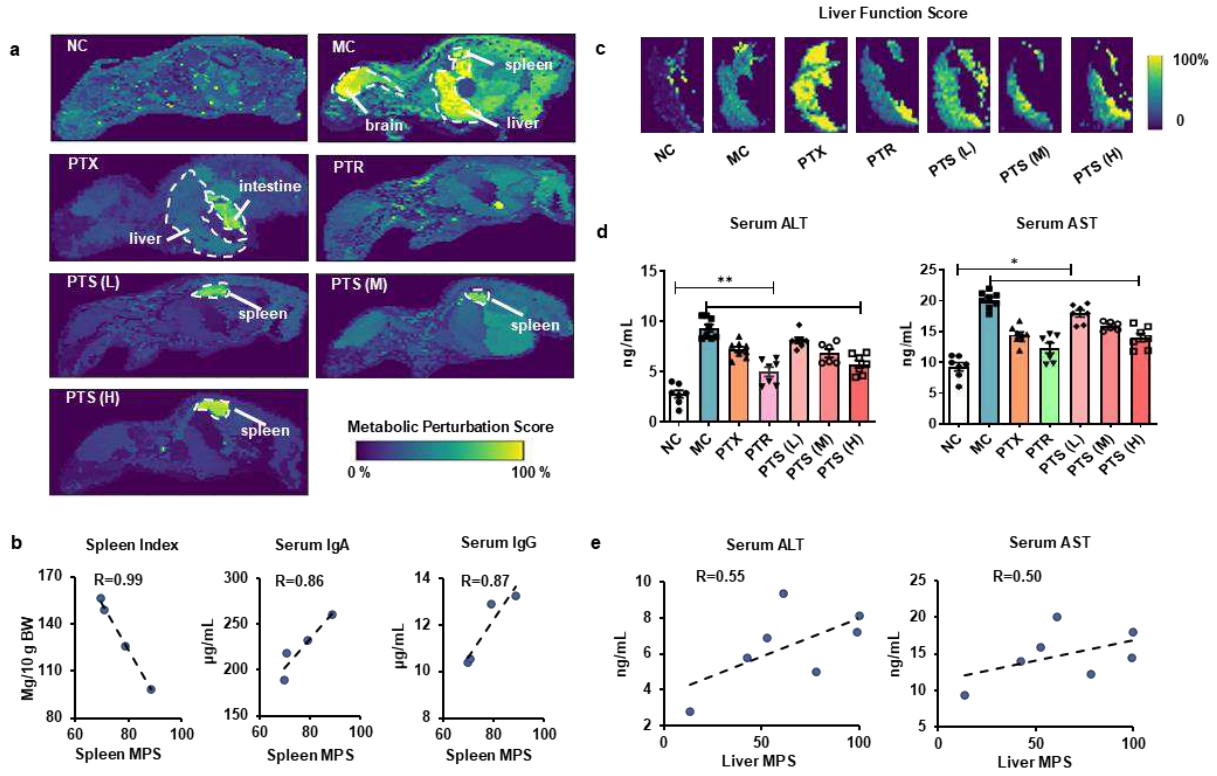

Fig.2. MSI$^{(x)}$ highlights the spatially resolved site of drug adverse effect and evaluates the organ physiological function. a Metabolic perturbation score images of different drug-treated WBA; **b** Correlation between spleen MPS values and spleen index and serum IgA, IgG. Serum IgA, IgG levels (n=7) were test by ELISA; **c** Metabolic perturbation score image to present the liver metabolism function. **d** ELISA results of serum AST and ALT concentration (n=7). **e** Correlations between liver MPS values and serum AST and ALT.

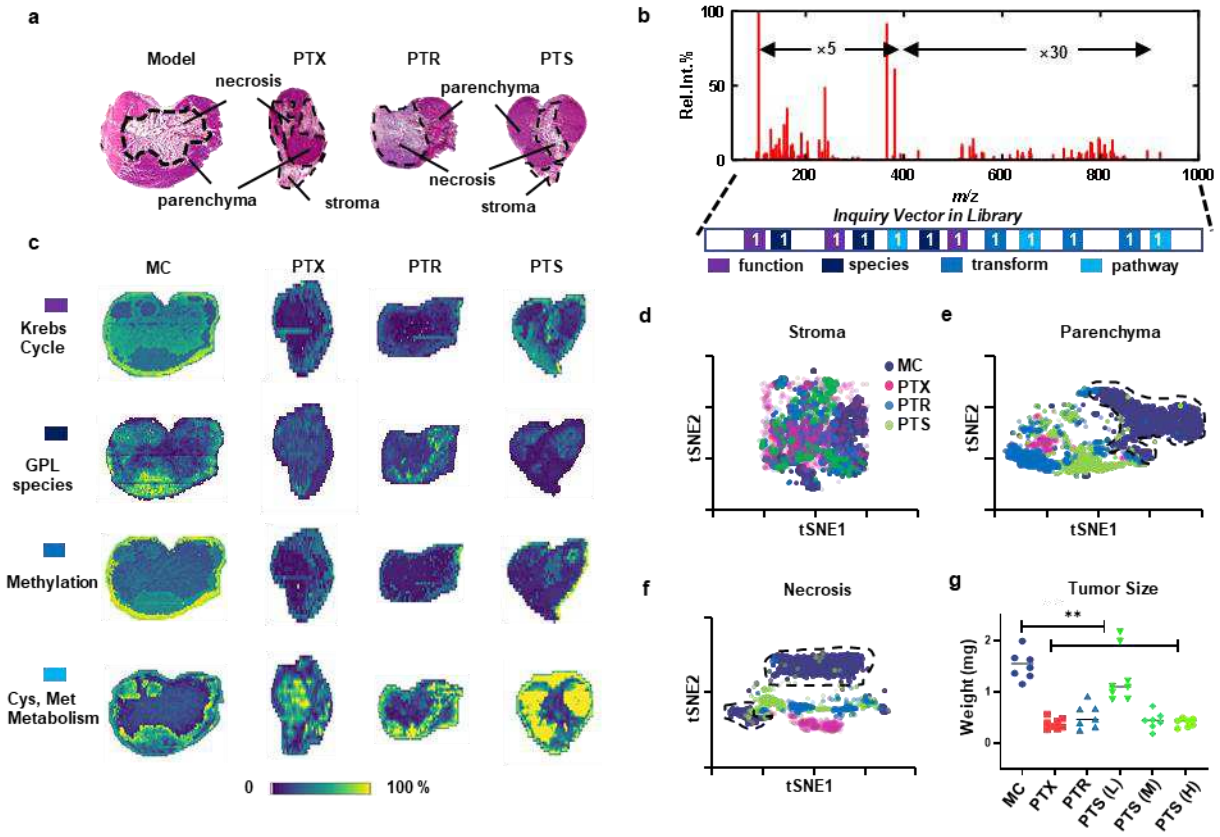

Fig.3. MSI$^{(x)}$ visualizes the tumor heterogenous metabolic response to the drug intervention. a H&E staining for tumor cryosections from different drug-treated groups. **b** Diagram of selecting a set of metabolite ions that belong to certain common search item such as function, species, biotransformation, or pathway. **c** Representative metabolic perturbation score images specific to certain search item in the high-order spatial metabolomics library. Cys, Met: cysteine and methionine metabolism; GPL: glycerophospholipids. **d-f** 2D t-SNE feature plots for characterizing tumor microregion-specific metabolic profile perturbation after drug treatment. **g** Weight of tumors collected from different drug-treated groups (n=7).

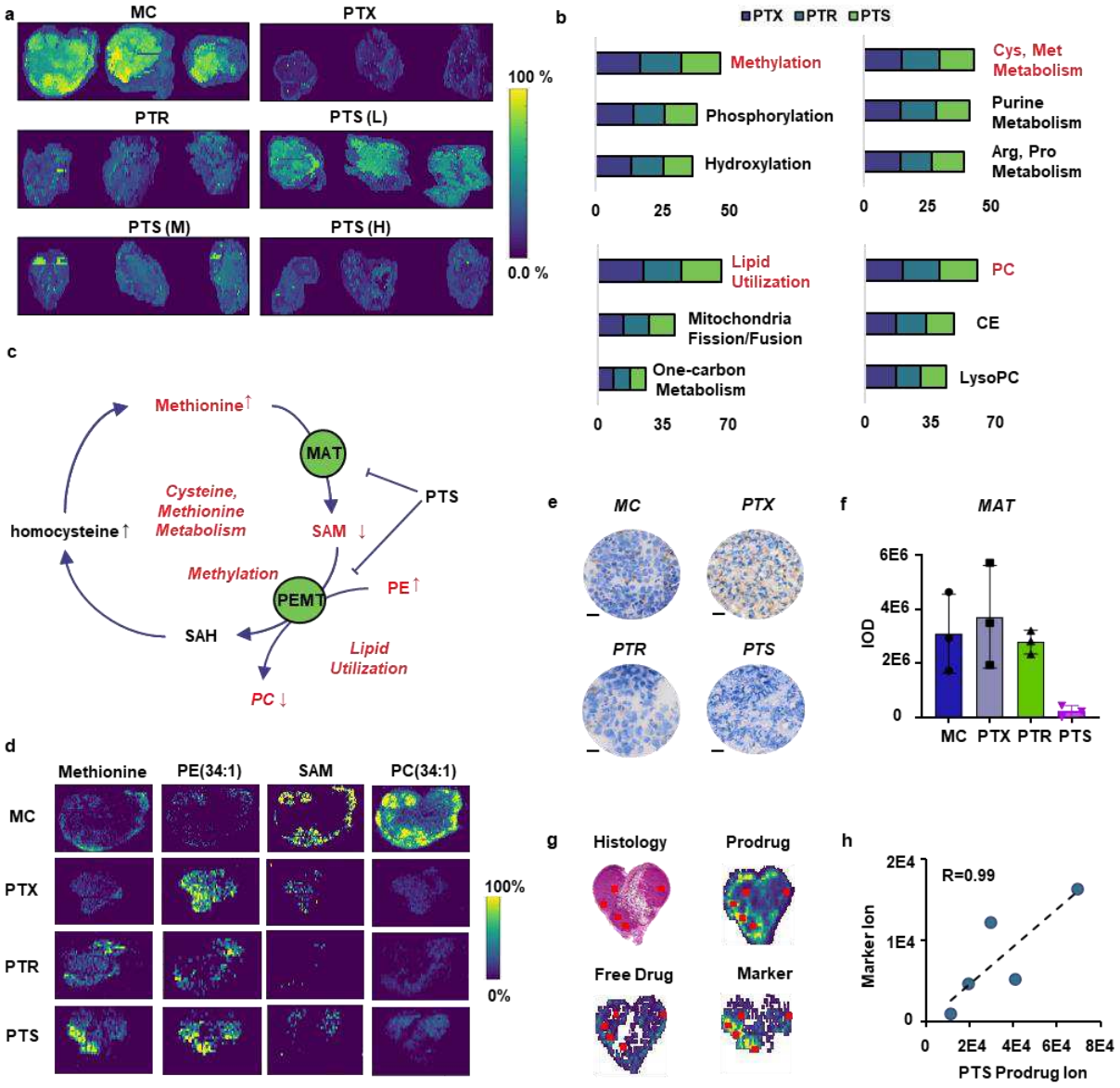

Fig.4. MSI$^{(x)}$ gains insight into the drug action mechanism and the potential drug target. a metabolic perturbation score images of tumor based on their untargeted metabolomics profile (n=3). **b** Top 5 pathways, species, biotransformation, and function items that were influenced after drug intervention. **c** postulated molecular mechanism for PTS anti-tumor effect. **e-f** biological validation of the MAT expression among different drug treated groups by immunohistochemistry (n=3). **g** Histological image of tumor from the PTS group and the MS image of PTS in the form of prodrug and free drug. The methionine was selected as the pharmaceutical marker for investigate the drug-marker spatial correlation. **h** correlation analysis for the drug and methionine.

Supplementary Files

This is a list of supplementary files associated with this preprint. Click to download.

- supplementaryinformation.docx